

Properties and Performance of Two Wide Field of View Cherenkov/Fluorescence Telescope Array Prototypes

S. S. Zhang^{a,*}, Y. X. Bai^a, Z. Cao^a, S. Z. Chen^a, M. J. Chen^a, Y. Chen^a, L. H. Chen^b, K. Q. Ding^a, H. H. He^a, J. L. Liu^a, X. X. Li^a, J. Liu^a, L. L. Ma^a, X. H. Ma^a, X. D. Sheng^a, B. Zhou^a, Y. Zhang^a, J. Zhao^a, M. Zha^a, G. Xiao^a

^a*Institute of High Energy Physics, CAS, Beijing 100049.*

^b*Hebei Normal University, China, Hebei 050016.*

Abstract

A wide field of view Cherenkov/fluorescence telescope array is one of the main components of the Large High Altitude Air Shower Observatory project. To serve as Cherenkov and fluorescence detectors, a flexible and mobile design is adopted for easy reconfiguring of the telescope array. Two prototype telescopes have been constructed and successfully run at the site of the ARGO-YBJ experiment in Tibet. The features and performance of the telescopes are presented.

Keywords: WFCTA, Cherenkov telescope, fluorescence telescope, Cosmic ray detector.

1. Introduction

The energy spectrum of primary cosmic rays spans almost 12 orders of magnitude, from 10^9 eV to 10^{21} eV, and can be well fitted by a simple power law except in several small energy regions. A region called the “knee” of the spectrum existing at around 10^{15} eV is one of these regions where the spectrum becomes steeper at higher energy side. Many experiments have observed this phenomenon; however, controversial arguments on its origin persist because of limited discrimination power on the primary cosmic ray composition and ambiguities in nucleus-nucleus interaction modeling. These two aspects are closely related to each other. Modern balloon borne experiments, such as ATIC [1] and CREAM [2], have efficiently measured the energy spectra of individual elements at the top of the atmosphere. The energy spectra for all nuclei are measured up to ~ 100 TeV which is not far from the “knee”. Because the detector area is constrained by the payload, the spectrum measurement has to be extended to a higher energy using a ground based air shower detector array. The spectrum should initially be measured well below 100 TeV to create an overlap with the balloon experiments which serve as absolute calibrations

for the ground-based techniques. Identifying the individual components of cosmic rays continues to be a major challenge in ground-based experiments. Multiple parameter measurements on an air shower seem to be a plausible approach. The ultimate goal is to separate individual species out of the total observed-event samples and measure a clear individual “knee” for every single species, enabling the discovery of the origin of the “knee”. As one of the major scientific goals of the Large High Altitude Air Shower Observatory (LHAASO) project [3, 4], the energy spectrum for a separated composition will be measured at energies above dozens of TeV. To tag each primary particle that causes an air shower, the atmospheric depth of the shower maximum should be measured as one of the important parameters. The wide field of view Cherenkov/fluorescence telescope array (WFCTA), one of the components of the LHAASO project, is designed to accomplish this goal.

A portable design of WFCTA telescopes is adopted to maximize the flexibility of changing the configuration of the array of telescopes. The elevations, pointing directions, and locations of the telescopes are then easily reconfigured. This is one way of using the same telescopes to serve as both fluorescence and Cherenkov detectors. In the fluorescence detector, the telescopes are tilted down to a horizontal position. In such an operational mode, which is analogous to the HiRes experiment [13], most of the Cherenkov photons are

*Corresponding author. Institute of High Energy Physics, CAS, Beijing 100049. Tel.: +86-010-88236035

Email address: zhangss@ihep.ac.cn (S. S. Zhang)

54 avoided except those that are scattered onto the field
55 of views (FOVs) of the telescope, such as in the fluo-
56 rescence detector of the telescope array experiment [10]
57 and the fluorescence detector of the Pierre Auger experi-
58 ment [8, 9]. Only the fluorescence light from the shower
59 is collected together with the scattered Cherenkov light
60 to trigger the telescopes. This requires showers hav-
61 ing much higher energy, usually above 100 PeV, such
62 as in the HiRes prototype experiment [15], because
63 the fluorescence light by a single electron is consid-
64 erably weaker and isotropic. In the Cherenkov detec-
65 tor, the telescopes run in high elevation mode to di-
66 rectly measure Cherenkov light from the showers, sim-
67 ilar to what was done in the Dice experiment [16]. A
68 Cherenkov light radiation provides considerably more
69 photons along the shower axis that are useful for lower-
70 ing the shower energy.

71 In 2007, two prototype Cherenkov telescopes [5, 6]
72 were deployed at Yangbajing (YBJ) Cosmic Ray Ob-
73 servatory near the ARGO-YBJ experiment [7]. More-
74 over, two WFCTA telescopes have been successfully
75 running in Cherenkov mode beginning August 2008. To
76 date, millions of cosmic ray events that simultaneously
77 trigger the telescopes and the ARGO-YBJ detector car-
78 pet array have been collected. An analysis of these
79 events is carried out to study the performance of the tele-
80 scopes. Detailed descriptions of the telescopes and the
81 analysis of the findings are presented in this paper.

82 Several details about the apparatus are presented in
83 Section 2. The detector calibration is then discussed in
84 Section 3. The test-run of the two telescopes and re-
85 sults are reported in Section 4 including summaries on
86 the detector performance. The conclusions drawn are
87 provided in the last section.

88 2. Apparatus

89 The two prototype telescopes are deployed near the
90 ARGO-YBJ carpet detector array at a longitude of
91 90.53°E, and a latitude of 30.11°N and 4300 m a.s.l.
92 One telescope is about 25 m away from the west side
93 of the ARGO-YBJ array. The other is also 25 m away
94 from the south side of the array with separation distance
95 between the two telescopes is 50 m. Each telescope has
96 an FOV of 14° in elevation by 16° in azimuth. The fo-
97 cal plane camera is made of a 16×16 photomultiplier
98 tube (PMT) array, and the pixel size is approximately
99 1°. Because both telescopes are tilted up to 60° point-
100 ing in the same direction, they can be operated in stereo-
101 scopic mode, i.e., showers striking an area covered by
102 the telescopes will be seen simultaneously. Since the
103 Cherenkov light from a shower is very concentrated in a

104 forward region; thus, the telescopes can be triggered by
105 showers coming within a cone of approximately 8° with
106 respect to the main optic axes of the telescopes.

The entire telescope system is composed of an op-
108 tic ultraviolet light collector, a focal plane camera, front
109 end electronics (FEE) based on 50-MHz flash analog-
110 to-digital-converters (FADC), data acquisition (DAQ)
111 based on an embedded ARM processor and PC104 bus,
112 power supplies for low and high voltages, and a slow
113 control system. Everything is installed in a shipping
114 container with dimensions of 2.5 m×2.3 m×3 m (Fig.1).
115 Mirrors are mounted at one end of the container and
116 the camera is located at the other end where the focal
117 planes of the mirrors are. The FEE and DAQ are placed
118 at the back plane of the PMT camera. A glass window
119 is installed at the entrance aperture to keep dust from
120 entering the apparatus. The container is mounted on a
121 dump-truck frame with a hydraulic lift that allows the
122 container to be lifted up from 0° to 60°. The mobility
123 of the entire telescope allows for freely switch between
124 configurations of the telescope array for different obser-
125 vational modes. The architecture of the electronic data
126 acquisition and the slow control system are shown in
127 Fig.2, whereas that of a sub-cluster is shown in Fig.3.
128 The PMT signals are processed using an analog process-
129 ing board (AB) and then a digitization board (DB). The
130 first level trigger (FLT) is generated in the DB on a sub-
131 cluster. After the FLT is determined, 256 FLT's are then
132 sent to the trigger board (TB). The second level trigger
133 (SLT) and the third level trigger (TLT) are then deter-
134 mined in the TB. After this, the event trigger from the
135 TB is fanned out by a bus driver board (BDB) and sent
136 back to each of the DB and GPS boards. The data are
137 initially stored in the buffer of the DB when the DB has
138 received the event trigger, after which the data that in-
139 clude the GPS time are read using TS7200. Finally, the
140 data are stored in a PC in the laboratory via Ethernet.
141 A detailed description of the detector, divided into the
142 following 8 subsystems, is provided: 1) optics, 2) cam-
143 era, 3) FEE, 4) trigger system, 5) DAQ, 6) power supply
144 system, 7) slow control system that includes monitoring
145 of everything, and 8) calibration.

146 2.1. Optics

147 A 4.7 m² spherical aluminized mirror, composed of
148 20 hexagon-shaped segments, is used as an ultraviolet
149 light collector. Each segment is subjected to a strict con-
150 trol of the surface quality and their geometrical and op-
151 tical properties. The reflectivity is greater than 82% for
152 light having a wavelength ≥ 300 nm. The radius of the
153 curvature of the segments is 4740 mm with a tolerance
154 of ± 20 mm.



Figure 1: Photograph of the telescope with the doors open.

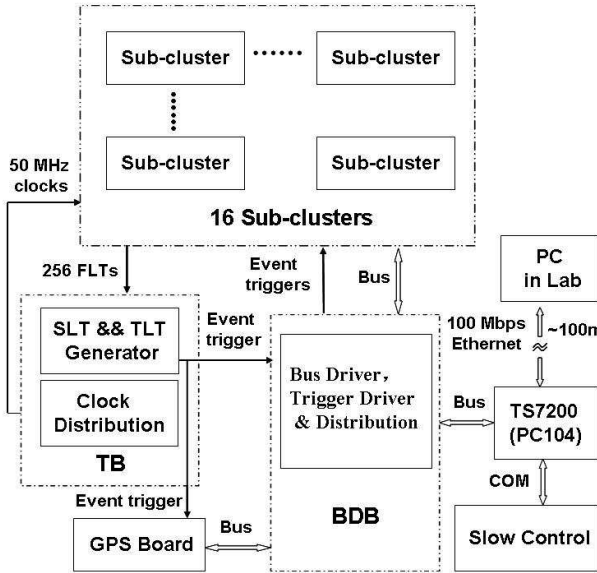


Figure 2: Communications diagram of one telescope; for details of the sub-cluster see Fig.3.

The size of a light spot on the focal plane where the PMT camera is located is designed to be similar to the size of a pixel. The sensitivity of a PMT is non-uniform across the surface of the photocathode [17], and small gaps exist between PMTs in the camera. For a spot that is exceedingly larger than the dimension of the gaps and the typical spatial scale of the non-uniformity across the photocathode, light from a specific direction will be shared by a few adjacent PMTs. Thus, effects stemming from the overall non-uniformity of response across the entire camera are reduced. The direction of incident

photons can be efficiently determined by simply taking the average of the directions of the registered pixels as weighted by the measured charge in a pixel. Contrastingly, the size of a spot is optimized to be similar to pixel size to avoid sharing of incident photons by an excessive number of pixels.

Because of the abbreviation of the spherical reflector, the spot size changes across the focal plane in a rather large FOV. Large comas also occur at large off-axis angles. The uniformity of the spot size over the camera is also optimized by locating the camera slightly away from the focus. A distance of 2305 mm between the mirror and the camera is eventually set according to a detailed ray-tracing calculation.

Each mirror segment is mounted on a spherical steel frame with three adjustable screws. The pointing orientations of all segments are adjusted toward the geometric center of the curvature. Using a laser beam, the orientations are calibrated to be less than 7.6 arc seconds from the nominal direction.

2.2. PMT Camera

Photons in a spot at the focal plane are recorded by a camera composed of 256 pixels which are 40 mm Photonis hexagonal PMTs (XP3062/FL). The camera is enclosed in a box and mounted on a frame at a distance of 2305 mm from the spherical mirror.

The PMTs in a telescope are operated at a gain of 6×10^5 . To achieve the best uniformity at hardware level, a resistor is placed between the high voltage power supply and each PMT base to compensate for the gain difference between PMTs. The gains (G) for all PMTs and their responses to the supplied voltage, i.e., $G \propto V^{-\beta}$, are calibrated. All β values are measured and recorded in a database in the laboratory for future use. The PMTs are then sorted according to their gains and grouped into two classes. For instance, the working voltages of the PMTs of one of the telescopes distribute 1088 V to the telescope in a common power supply with a variance of 73.97 V. The average β of these tubes is 5.9 with a variance of 0.6.

The 16 PMTs, as an integrated unit, are soldered on a high voltage board (HVB) that distributes a negative high voltage to all cathodes and dynodes of the PMTs. The voltage division scheme is recommended by Photonis to yield the maximum gain of the tubes. The maximum output current of the PMTs allows a range of 3.5 orders of magnitude in which the non-linearity of all tubes is less than 8% according to a calibration in the laboratory [17]. The anode signals are finally DC coupled to the FEE.

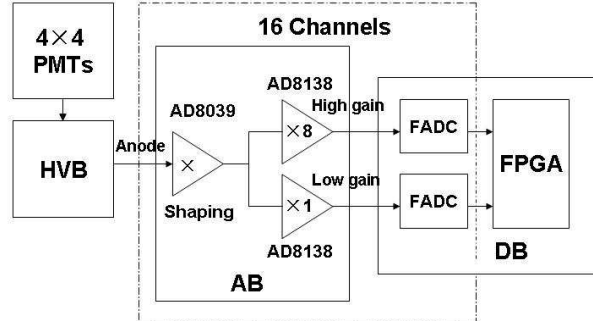
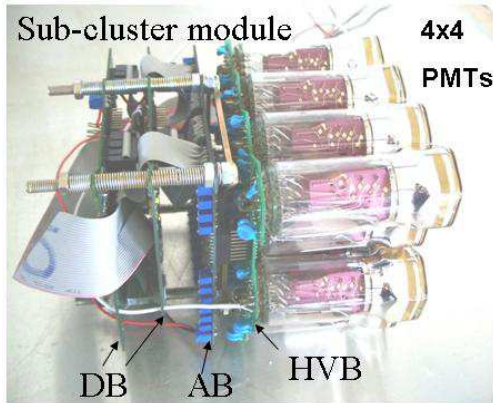


Figure 3: Photograph of a sub-cluster (left) and schematic of the sub-cluster (right).

2.3. FEE and Digitization

The FEE is located behind the HVB, which is composed of an AB and two DBs, to avoid a long distance transmission of the analog signals. Such a module is referred to as a sub-cluster (see the left figure of Fig.3) in this paper. A block diagram on the procession of signals from the PMTs to the on-board data storage chip is shown in the right figure of Fig.3. The signal of each PMT is transmitted to the first amplifier on the AB for noise filtering and pulse stretching. Upon division into high or low gain channels, the signal is then sent to the DB for digitization and further processing. The rest of this section describes the processing procedure in detail.

2.3.1. Analog Processing Board

Each AB has 16 channels for the signals from 16 PMTs on HVB alone. Each channel has a shaping circuit and amplifiers for low or high gains. The board has four main functions, namely:

- low-pass filter of 20 MHz,
- expanding narrow pulses,
- dual-gain system for covering a dynamic range over 3.5 orders of magnitude,
- and receiving PMT signals from HVB and performing a single-ended-to-differential conversion.

The anode signals are fed to a four-pole low-pass filter based on an AD8039 through DC coupling. Cherenkov photons generated by all shower particles move at almost the same speed as the charged particles; thus, all photons generated over the entire shower development beginning from the top of the atmosphere hit the cathodes at almost the same time. The duration of

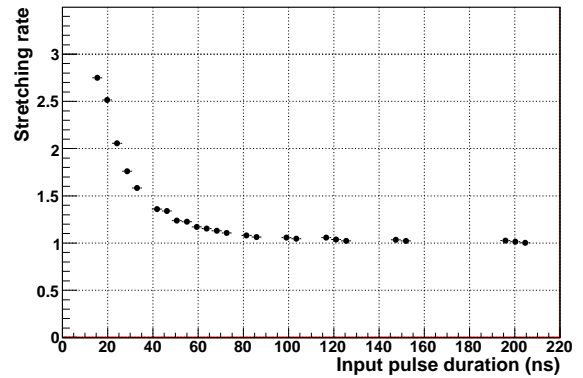


Figure 4: Stretching ratio as a function of the input pulse duration.

the pulse lasts only a few nanoseconds, which is shorter than the typical response time of the PMT, e.g., a pulse duration generated by a single-photo-electron (SPE) is approximately 12 ns on average. Therefore, such a narrow pulse has to be stretched (e.g., at > 50 ns) to be able to measure the charge at a sampling rate of 50 MHz, as preselected for the FADCs on DBs. Taking into account the optimized bandwidth of the noise filter, the stretching ratio is selected in such a manner that the narrower pulses are stretched further, and pulses wider than 120 ns are essentially not stretched. In Fig.4, the stretching ratio is plotted as a function of the pulse duration. According to this, the original waveform is reconstructible, and the timing of the pulse can be corrected with an uncertainty less than the duration of the stretched pulses.

The amplification of the PMT signals with a gain of 2.67 is another feature of the shaping circuit. The value of the gain is also optimized together with the filter and

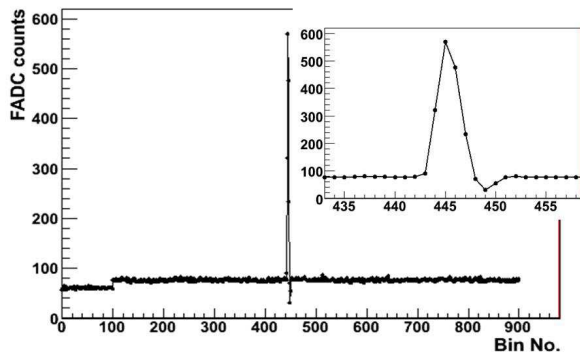


Figure 5: A Cherenkov signal with sky background; the first 100 bins are low gain background and the remaining 800 bins are high gain background and the Cherenkov signal. The Cherenkov signal is in the current frame (from the 300th bin to the 600th bin).

the stretcher. The AD8039 has a sufficiently high speed (350 MHz), low power dissipation, low cost, low noise, low distortion, and a nonlinearity less than 1% in a range of the input from 0.5 mV to 800 mV, which nearly fits the entire range of the PMT signals.

To maintain good linearity over a wide dynamic range of 3.5 orders of magnitude in charge, a dual gain system is designed. Signals coming out of the AD8039 are split into two channels and are then separately amplified by two AD8138. With such a design, considerable flexibility in obtaining different resolutions of the charge measurements for pulses with different pulse heights is achievable by choosing the range covered by the high gain channel. In this paper, a ratio of the gains of 1:8 is selected as a result of the optimization between the dynamic range and the resolution in the charge measurement. The nonlinearity of AD8138 is less than 2% at both gains of 1 and 8 in the entire range of the input signals.

Another excellent feature of the AD8138, the conversion between a single-ended input and differential output for instance, makes it the best choice for an amplifier. Superposing an offset to the output of the AD8138 as a pedestal of the signal before feeding into the positively-polarized FADC is also a convenient approach. To manage possible undershoot of the pulses (see Fig.5), a pedestal is preset higher than the undershoot.

2.3.2. Digitization Board

Each DB has 8 pixel channels, which includes 16 FADC modules managed by two field programmable gate array (FPGA) modules. The 10-bit FADCs, AD9215, has a good cost-performance ratio with a lin-

earity better than 2% over a range of 40 to 900 counts. However, it is not sufficient to cover the required dynamic range of the detector. Two FADCs are then used for the dual gain system. At an input range of 2 V, the FADC continuously digitizes analog signals with a sampling rate of 50 MHz (20 ns/bin) and a resolution of 2 mV per count. In the dual gain system, a range of 0 to 500 photoelectrons with a resolution of 1.7 counts per photoelectron is set for the high gain channel, whereas a range of 0 to 4000 photoelectrons with a resolution of 0.21 counts per photoelectron is set for the low gain channel.

A digitized waveform is collected by an FPGA, Xilinx XC3S1000, and fed into a pipeline with a length of 1500 clock cycles. Every 300 cycles is defined as a frame in which a single channel trigger is formed. Such a long pipeline enables an enduring waveform waiting for global trigger formation and transmission. This pipeline also allows three frames, i.e., previous, current, and post ones, to be recorded once a global trigger is received. This guarantees storage of a complete waveform regardless of when the pulse starts in the "current" frame.

The FPGA also makes a choice between the signals from high gain and low gain channels when the bit stream flows in. Any signal higher than 900 counts triggers a switch from the high gain channel to the low gain channel. This way, an effective overall dynamic range of 12 to 13 bits is achieved.

2.4. Trigger system

A final trigger among the telescopes is determined based on the three trigger levels, namely, the single channel trigger (the lowest level), telescope trigger (the second level), and event trigger (the highest level). The topology of the three-level trigger algorithm is outlined in Fig.6, with corresponding details discussed in following subsections.

2.4.1. First Level Trigger in a Single Channel

The FLT is formed in the FPGA located on the DBs provided that the signal-to-noise ratio in a window is greater than a given threshold (e.g., 4 as a typical value). The width of the window is predetermined for corresponding observation modes (e.g., 8 bins for the Cherenkov light signals). Running over the entire frame of 300 cycles once in a bin, 293 sums of FADC counts in the windows (denoted as WINSUM) are produced. The average of WINSUM is calculated using these WINSUMs avoiding the maximal WINSUM and

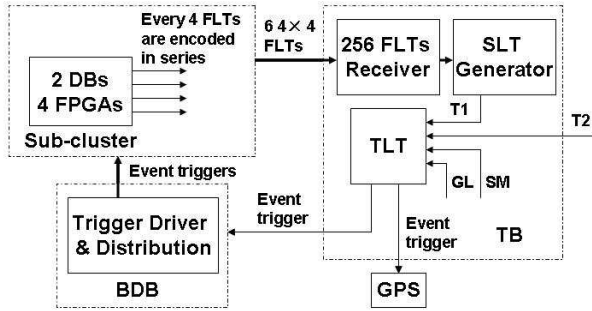


Figure 6: Three-level trigger system. SM is stereo or mono enable signal, GL is global or local enable signal, T1 is the telescope trigger from telescope No. 1 and T2 is from telescope No. 2. See detailed explanation of the diagram in the text.

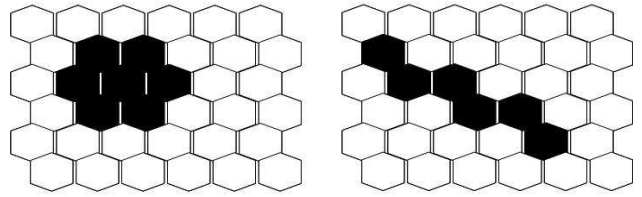


Figure 7: Two typical patterns in the second level trigger.

18 WINSUMs on each side of the maximum. The standard deviation (σ) of the WINSUM around the average serves as a measure of the background fluctuation. If the maximum of WINSUMs exceeds the average by $n\sigma$, the FLT is formed, where n is preselected from a list of $\sqrt{12}$, $\sqrt{16}$, $\sqrt{24}$, $\sqrt{32}$ and $\sqrt{40}$ before starting the run. All trigger signals from 64 FPGAs are encoded into bitmaps and transmitted to the Trigger Board (TB) in parallel (see Fig.6).

The frame size of 300 bins is selected for a full scale array with more than 24 telescopes covering an area of 1 km^2 , over which a highly inclined air shower takes several microseconds to cross in the fluorescence light observational mode. Such a frame is large enough to fully contain the entire shower; it is also large enough for Cherenkov light. All Cherenkov photons arrive at the telescopes at almost the same time (few ns). Therefore, an air shower signal appears only within 5 or 6 bins after shaping and the night sky background is measured in the rest of the frame (see Fig.5). Such continuous measuring of the sky background is highly useful not only in estimating the signal-to-noise ratio but also in monitoring the transparency of the atmosphere using well-known bright stars in the field of view.

2.4.2. Second level trigger for a single telescope

A trigger for a telescope registered by an air shower (denoted as second level trigger or SLT) is formed when a specific pattern of triggered PMTs corresponding to a possible air shower is found in the camera of a telescope. A pattern recognition technique, developed in the Pierre Auger experiment [11] that is operated in a FPGA located on the TB, is applied. Numerous patterns, such as a fully filled circle formed with one hexagonal pixel surrounded by six others, or a straight line formed by six aligned pixels, are pre-loaded into the

FPGA as a look-up table. Once all 256 FLT signals are collected, the FPGA matches all the pre-stored patterns with the observed one within a 6×6 matrix of pixels. Moreover, it keeps such a box running throughout the entire PMT camera with a step of one row or one column. The SLT is formed as long as any one of the pre-stored patterns is matched. According to the simulation for air showers, mainly two types of patterns exist. Fluorescence light images of air showers seen from several kilometers away tend to form line-shaped patterns on the camera, whereas Cherenkov light images of showers hitting the telescope head-on tend to form round-shaped patterns, as shown in Fig.7. There are 16 round-shaped patterns and 729 line-shaped patterns in a 6×6 box.

To speed up the formation of SLT, the pattern comparisons in the box are conducted in parallel. All 121 bitmaps of the boxes are generated by sliding the box are done in parallel. All 121 bitmaps of the boxes are generated by sliding the box throughout the camera. A pattern comparison algorithm is then carried out among the 121 bitmaps. The telescope trigger (SLT) is formed in 123 clock cycles, i.e., $2.46 \mu\text{s}$.

2.4.3. Third level trigger for entire array of telescopes

An event trigger for the entire array of telescopes (denoted as the third level or TLT) is generated using one of the FPGAs used for SLT. For the two prototype telescopes, only two modes, namely, stereoscopic and monocular observation of showers, exists if they are configured in such a way that the two telescopes have a maximal overlap of the FOV. In stereoscopic mode, the two telescopes are required to simultaneously observe a shower. In monocular mode, each of the two telescopes can trigger the entire site. The operational mode should be selected at the beginning of a run by assigning two controlling parameters, SM and GL, as marked in Fig6.

The two telescopes communicate with each other through a two 80 m coaxial cables by sending telescope

419 triggers (SLT) out and receiving the event trigger (TLT). 469
420 Such a trigger function is also useful for receiving an 470
421 external trigger and delivering a trigger to other co-sited 471
422 detectors. This makes the telescope an open and modu- 472
423 larized system. 473

424 2.5. DAQ system 474

425 The philosophy of the design of the Cherenkov tele- 475
426 scope DAQ is integrated and compact so that the en- 476
427 tire DAQ can be arranged on the backboard of the focal 477
428 plane camera. It allows for the maximal mobility of the 478
429 telescope for flexibility in switching between configura- 479
430 tions. Because of the limited space, a low power con- 480
431 suming and compact-embedded online computer based 481
432 on an ARM processor, industrial standard PC104 bus, 482
433 and flash disk are selected as the backbone of the DAQ 483
434 system, eliminating the need for moving parts such as 484
435 the CPU fan and hard drives. All of the components are 485
436 integrated on a bus driver board, which bridges the data 486
437 storage disk and the 32 DBs that are connected by flat 487
438 cables. Because the event rate is not extremely high, 488
439 i.e., around 1 Hz, a band width of 14 MHz for a PC104 489
440 bus is sufficient for transferring every bit of the $6\ \mu\text{s}$ long 490
441 wave forms to the disk for all 256 channels. It is also ex- 491
442 tremely advantageous for system debugging. Each tele- 492
443 scope is an independent detector with a complete DAQ 493
444 system on board. The communication with the rest of 494
445 the experiment is through a 10/100 Mbps Ethernet. 495

446 Each telescope has its own independent DAQ, devel- 496
447 oped using C++ language under Linux. Operating in 497
448 a polling mode instead of an interrupt mode, the DAQ 498
449 checks the interface status regularly for whether the data 499
450 are ready or not. If so, the data in the buffer are read 500
451 and immediately stored in the disk. Before a night shift 501
452 ends, the data in the hard disk are moved to the Institute 502
453 of High Energy Physics (IHEP) in Beijing for further 503
454 analysis. 504

455 2.6. Power supply, slow control, and status monitoring 504

456 The two power supplies with +7 V (maximum current 505
457 80 A) and -7 V (maximum current 20 A) are installed in 506
458 the container. Regulators are used at each AB and DB 507
459 to further stabilize the voltage. An adjustable HV power 508
460 supply with a maximal output of -2000 V and 100 mA 509
461 is used for each telescope. 510

462 One of the difficulties at high altitudes is the heat dis- 511
463 sipation of the power supplies and electronics enclosed 512
464 in a metal box. The total power consumption is about 513
465 50 A at +7 V and 16 A at -7 V. A forced cooling sys- 514
466 tem is necessary in the prototype experiment to improve 515
467 the heat dissipation of the entire camera and the power 516
468 supplies. 517

The entire telescope system is powered by an unin-
interrupted power supply with a sufficient battery backup.
It protects the telescopes from damage when a blackout
occurs.

The detector is designed to work in remote control
mode, including the opening and closing of the doors,
turning the power supplies on/off, enabling/disabling
the high voltage (HV) power supply and low voltage
(LV) power supplies, and switching the UV LEDs on/off
for detector calibration. All kinds of controls are real-
ized using the on-board computer through a COM port.
Carefully monitoring the status of each telescope is nec-
essary, including the door status, voltages, and tem-
peratures at different places (e.g., enclosed areas inside
the camera, backboard of the PMT camera, and inside
the housing of the UV LED). All parameters are mea-
sured and recorded through an 8-channel 12-bit analog-
to-digital-converter on the board of the embedded com-
puter, TS7200.

All of the controls are performed through a user in-
terface running at the embedded computer connected
through Ethernet from an operational center, 3000 km
away in IHEP in Beijing. A small portion of the data
can be copied to display the event during the operation.

518 3. Calibration 518

519 3.1. Method of calibration 519

520 An accurate shower reconstruction requires a con- 520
521 verting factor from a pulse area in terms of FADC 521
522 counts to the number of photons for each pixel. There- 522
523 fore, the absolute calibration of the detector response is 523
524 essential. To achieve this objective, having an accurate 524
525 knowledge about PMT cathode effective areas, cath- 525
526 ode quantum efficiency, PMT gains, amplifier gains, 526
527 and digital converting factors, is necessary. Measur- 527
528 ing all these effects item by item is difficult. In this 528
529 paper, a method similar to the HiRes experiment [14] 529
530 and Pierre Auger experiment [12] calibration procedure, 530
531 which considers the entire effect, is applied to measure 531
532 the overall response of each pixel. The procedure is dis- 532
533 cussed in the paragraphs that follow. 533

534 Being mounted at the center of the mirror, a UV-LED 534
535 (375 nm) light source with a diffuser is used for the cal- 535
536 ibration of PMTs in the camera by beaming nearly uni- 536
537 form light to every pixel. The LED light density on the 537
538 camera surface is calibrated using a pre-calibrated probe 538
539 detector located beside the camera. The calibration of 539
540 all pixels in the cameras is performed twice a day, i.e., 540
541 before and after the daily operation. The crucial part is 541
542 the measurement of the absolute number of UV photons 542

518 at each PMT cathode from a pulse emitted by the LED,
 519 which is performed in two steps.

520 First, we move one PMT over all the places on the
 521 frame of the PMT camera to measure the uniformity of
 522 the LED light density on the camera surface. This has
 523 to be accomplished before the PMT camera is installed.
 524 The light density is a function of the polar angle, θ , in a
 525 form of $\cos^4\theta$, where θ is the angle between the connec-
 526 tion from the LED to the PMT location and the perpen-
 527 dicular connection from the LED to the PMT camera
 528 surface. The variation from the center to the corner of
 529 the PMT camera is within 7%.

530 In the second step, the light density is measured using
 531 a pre-calibrated probe consisting of two XP3062 PMT's
 532 with the same FEE and DAQ as the two telescopes. The
 533 only difference is that the two PMT's in the probe are
 534 operated at a very high gain so that the single photoelec-
 535 tron can be measured. Therefore, the gain of the probe,
 536 G^{probe} , can be calibrated at any time. Then, the absolute
 537 calibration of the probe is performed at the HiRes lab
 538 at the University of Utah, USA, by comparing the re-
 539 sponse of a hybrid photo diode (HPD) pre-calibrated at
 540 NIST [18] to the same light source. The probe and HPD
 541 are located side by side in front of a UV-LED at 355 nm.
 542 Using the HPD, we measure light density I_U (number of
 543 photons per square millimeter) from the LED. We also
 544 measure pulse area F_U^{probe} using the probe simultane-
 545 ously. At the operational site in Tibet, the light density
 546 from the LED mounted on the center of the mirror is
 547 calibrated to be $I_T = I_U \frac{F_T^{probe} G_U^{probe}}{F_U^{probe} G_T^{probe}}$, where U and T stand
 548 for Utah and Tibet, respectively.

549 Applying the knowledge obtained from the two steps,
 550 we have determined both the light density in front of
 551 the cathode and the pulse area in terms of the FADC
 552 counts for each PMT in the camera. Finally, the over-
 553 all converting factor for a pixel between the number of
 554 photons reached to the surface of the camera and cor-
 555 responding pulse area measured by the FADC counts
 556 behind the pixel is

$$557 \quad C_{375}^{camera} = \frac{F_T^{camera}}{I_T A_{PMT}} \frac{\cos^4\theta^{probe}}{\cos^4\theta^{camera}}, \quad (1)$$

558 where A_{PMT} is the geometric area of the PMT cathode,
 559 and C_{375}^{camera} is the calibration constant for a pixel. The
 560 subscript 375 indicates that the calibration is done using
 561 UV light at 375 nm. The unit of the calibration constant
 562 is FADC counts per photon. θ^{probe} and θ^{camera} represent
 563 the angular locations of the probe and the pixel in the
 564 camera, respectively. A further correction according to
 565 the wavelength dependence of the quantum efficiency
 566 of PMT's is applied in the operation for the cosmic ray
 567 observation.

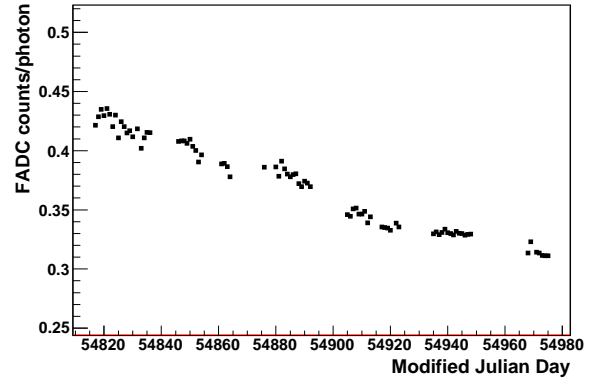


Figure 8: Absolute gain of one telescope from Dec. 2008 to May 2009, as a function of time.

568 3.2. Result of the calibration

569 The probe was calibrated at the HiRes lab. The cali-
 570 bration results are shown in table.1; the gain of the probe
 571 is 85.7 ± 0.3 FADC count per SPE. The second column
 572 shows the lower LED photon density and the third col-
 573 umn shows the higher LED photon density that coincide
 574 with one another.

Table 1: The calibration results of the probe.

$I_U(\text{photons}/\text{mm}^2)$	$0.359 \pm 4.8\%$	$0.538 \pm 4.8\%$
$F_U^{probe}(\text{FADC count})$	8959 ± 4	13650 ± 5

575 The corresponding calibration constant for one of the
 576 telescopes is presented in Fig.8. An average of the cali-
 577 bration constants of all pixels in the camera is plotted
 578 with respect to time from December 2008 to May 2009.
 579 As mentioned above, the calibration constant is moni-
 580 tored every observational day. The systematic uncer-
 581 tainty of the calibration constant is estimated to be 7%.
 582 The downtrend of the constant shown in the figure indi-
 583 cates obvious decreases of gains in all newly produced
 584 of PMT's. The transmission of the glass window and re-
 585 flectivity of the mirrors are not take into account in the
 586 above calibration. These two effects will be monitored
 587 in so called end-to-end calibration using nitrogen laser
 588 in future.

589 4. Performances and Results from Test Run

590 4.1. Test Run Information

591 The two telescopes began recording cosmic ray data
 592 in August 2008. Furthermore, both monocular and
 593 stereoscopic modes have been tested. About 500,000

594 coincidental events with the ARGO-YBJ experiment
 595 in stereoscopic mode and 700,000 coincidence events
 596 in monocular mode have been collected up to January
 597 2010. The average trigger rate is about 0.5 Hz in stereo-
 598 scopic mode and 0.7 Hz in monocular mode.

599 4.2. Off-line Coincidence with the ARGO-YBJ Experi- 600 ment

601 All WFCTA telescopes and the ARGO-YBJ experi-
 602 ment recorded the cosmic ray arrival time based on a
 603 GPS. A time window of $8 \mu\text{s}$ containing a Cherenkov
 604 event is searched for coincidence with the ARGO-YBJ
 605 event stream, which is about 4 kHz. A difference be-
 606 tween the recorded event time by the two experiments
 607 for a matched event is typically less than 100 ns (Fig.9).

608 For a coincidence event, the shower geometry is mea-
 609 sured using the ARGO-YBJ detector. The distribution
 610 of shower arrival directions is shown in a 2-dimensional
 611 map, i.e., zenith angles versus azimuth angle, as in
 612 Fig.10. Approximately 85% of coincident events occur
 613 inside the FOV of the Cherenkov telescopes marked by
 614 the trapezium. The rest of the 15% of events have their
 615 images partially seen by the telescopes and sufficiently
 616 trigger the telescopes. The shower core distribution is
 617 shown in Fig.11. The ARGO-YBJ experiment array and
 618 the two Cherenkov telescopes are marked as the rectan-
 619 gle and two dots in the figure, respectively. For events
 620 that have the reconstructed cores inside the ARGO-YBJ
 621 array, the shower parameters, such as the number of hits
 622 on the carpet detector (N_{hit}) and shower geometry, are
 623 well measured. A distribution of N_{hit} of these events is
 624 plotted in Fig.12. According to the number of hits as a
 625 function of the primary energy of proton from ARGO-
 626 YBJ detector [19], the mode energy of protons is about
 627 40 TeV. This estimates the threshold of two Cherenkov
 628 telescopes in stereoscopic mode.

629 In Fig.13, two Cherenkov images are shown in the
 630 event display. The top image is caused by an event at
 631 a $10 \text{ m } R_p$ (the impact parameter of the shower to the
 632 telescope) and the bottom image stems from an event at
 633 a $173 \text{ m } R_p$. The image is clearly more elongated for the
 634 farther event. Using the well-defined image parameters
 635 created by Hillas [21], length and width, this effect is
 636 more quantitatively presented in Fig.14. The widths of
 637 the images seem to be no longer shrinking once show-
 638 ers are sufficiently far from the telescopes (e.g., farther
 639 than 100 m). The showers essentially resemble linear
 640 patterns.

641 4.3. Electronic noisy and sky background

642 For a triggering system completely based on the
 643 signal-to-noise ratio, such as the WFCTA telescopes,

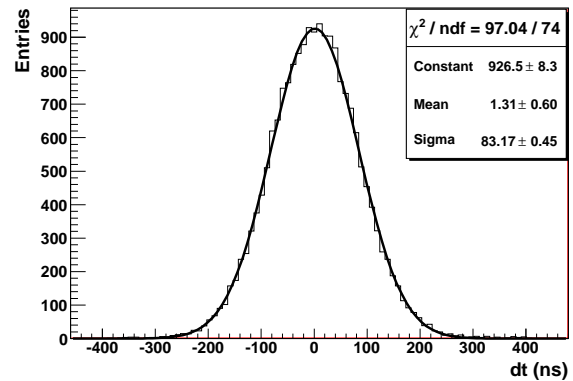


Figure 9: The difference time between WFCTA and ARGO in coincidence event.

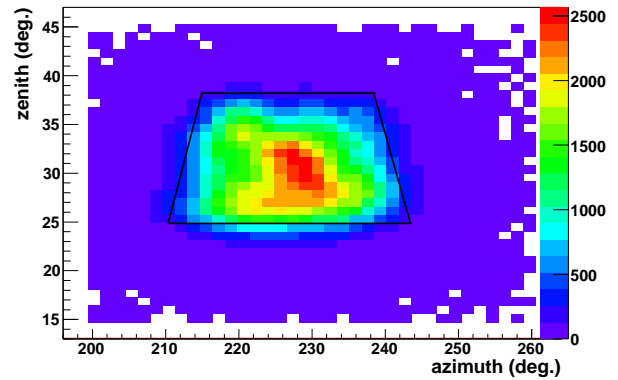


Figure 10: Distribution of coincidence events are seen by ARGO and Cherenkov telescopes simultaneously over zenith and azimuth angle. About 85% of coincidence events are located in the Cherenkov telescope FOV (trapezium). The image of the rest of the 15% of coincidence events is partially in the Cherenkov telescope FOV.

644 the sensitivity is constrained by the noise level. For a
 645 most optimized system, the electronic noise must be
 646 negligible compared with the night sky background.
 647 Both of them are measured during the operation as the
 648 door is closed and opened, respectively.

649 The sources of electronic noise include thermal
 650 noises in the PMTs, noises from the HV power supply
 651 and LV power supplies, noises of amplifiers, and finally
 652 from the counting error of FADCs. The PMT Photonis
 653 XP3062/FL has a very low dark current; therefore, the
 654 thermal noise level is sufficiently low so that it can be
 655 ignored compared with the other sources of electronic
 656 noises. The HV power supply has a ripple less than
 657 0.02% in terms of RMS of rated voltage. This con-
 658 tributes a variation within 0.12% in terms of the gain
 659 of the PMTs. Voltage regulators are used to block pos-

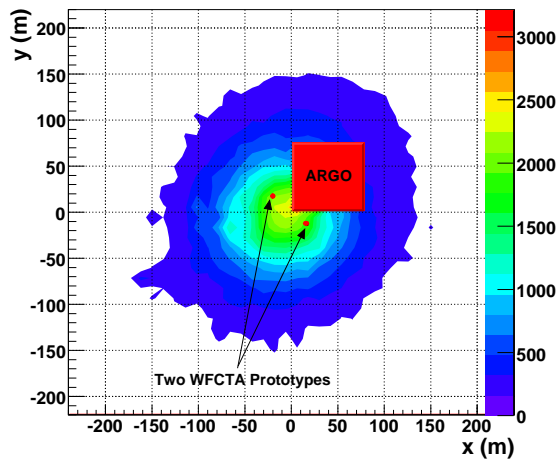


Figure 11: Distribution of shower core. Two Cherenkov telescopes (two dots) and the ARGO-YBJ experiment array (rectangle) are also marked in the figure.

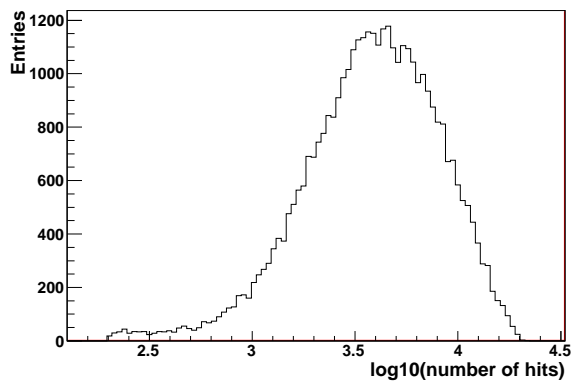


Figure 12: Distribution of ARGOn hit of these coincidence events, whose reconstructed core is located in the ARGO-YBJ cluster array.

660 sible noises from the LV power supplies. All ampli- 676
 661 fiers, AD8138 and AD8039, are selected to generate 677
 662 a very low noise level. The noise from the FADC is 678
 663 about 0.5 FADC counts per tube. Taking into account 679
 664 all additional sources such as the distributing capacity 680
 665 on boards and connectors, the total electronic noise, 681
 666 including PMT and high voltage power supply, is typi- 682
 667 cally about 1.0 FADC counts per tube. It is measured 683
 668 during the calibration with the LED (Fig.15) as long as 684
 669 the signal is avoided. 685

670 The night sky background is measured similarly as 686
 671 a shower trigger is formed when the doors are open 687
 672 (Fig.5). The fluctuation in the night sky back-ground 688
 673 is typically more than 2.2 photon electrons per 20 ns per 689
 674 tube on a clear moonless night. This suggests a much 690

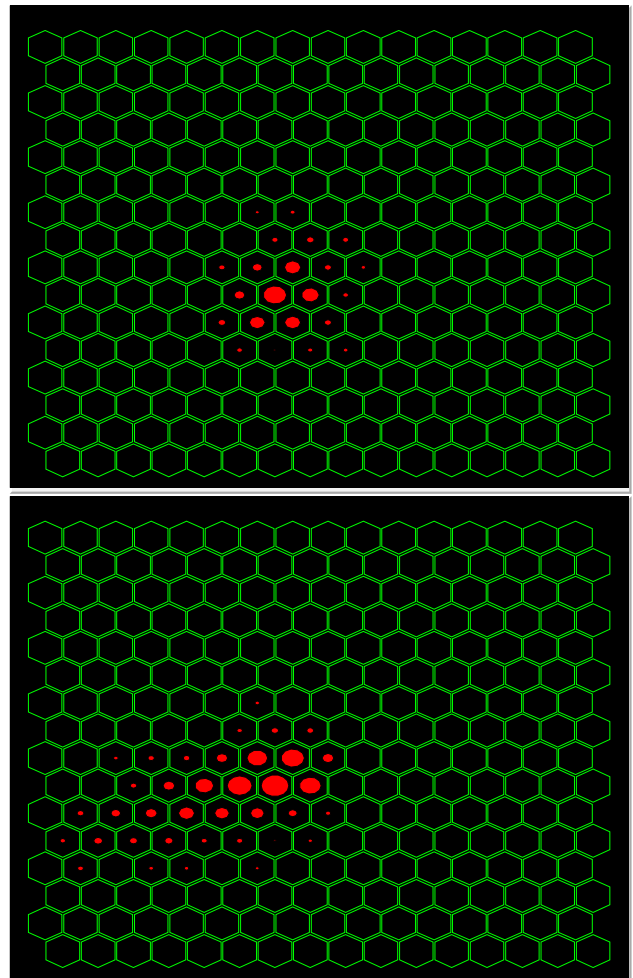


Figure 13: Two Cherenkov events; the R_p of the tope event is 10 m and that of the bottom event is 173 m; the image of the bottom event has a longer tail than the top event.

675 stronger noise than electronic noises. One of the impor-
 676 tant sources of the sky background is light from the stars
 677 (Fig.16), which shows the sky background at night, in
 678 which each pulse denotes stars passing through the FOV.
 679 A bright individual star can be traced when it passes
 680 through the telescopes. Stars provide numerous stable
 681 point-like sources that typically sweep across a tube in
 682 about 4 minutes. Those ideal point-like sources can be
 683 used for multiple calibration purposes. For instance,
 684 well-known bright stars can be used as light houses to
 685 establish the pointing direction of the telescope itself,
 686 with accuracy proved to be better than 0.05° [20]. A
 687 bright star can be seen as a very stable point-like source
 688 at infinity, which is a perfect tool for measuring the spot
 689 size produced by the optical system. The background
 690 of a tube signal steadily increases when the light spot

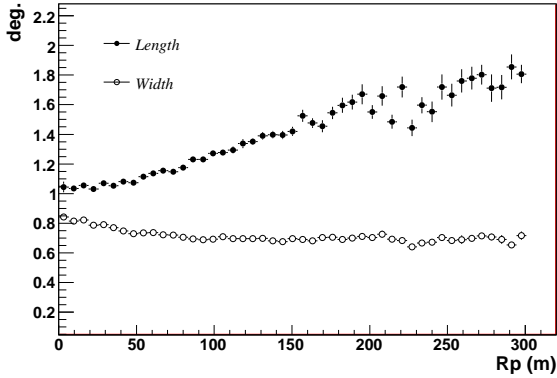


Figure 14: Length (filled circles) and width (open circles) as a function of Rp.

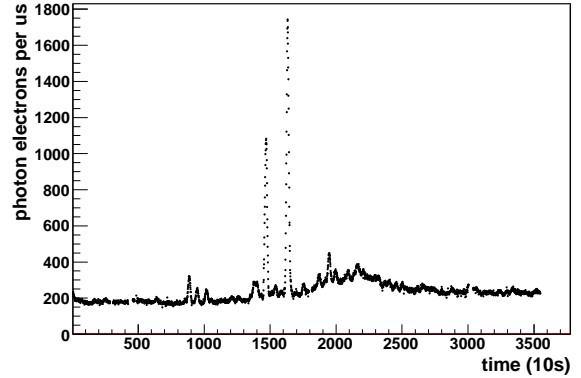


Figure 16: Sky background is monitored by a PMT in a clear moonless night; each pulse corresponds to a star passing through the FOV of the telescope.

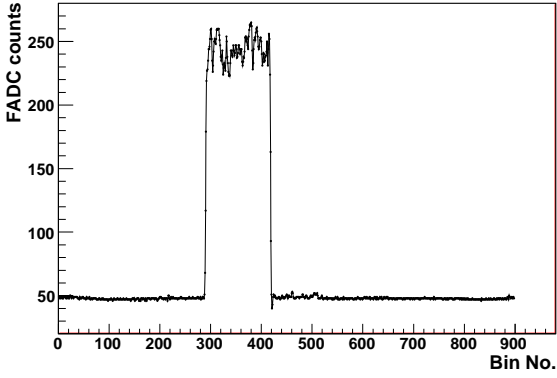


Figure 15: LED calibration for door closed. The low noise level of 1 LSB of the complete electronics is to be seen before and after the LED pulse.

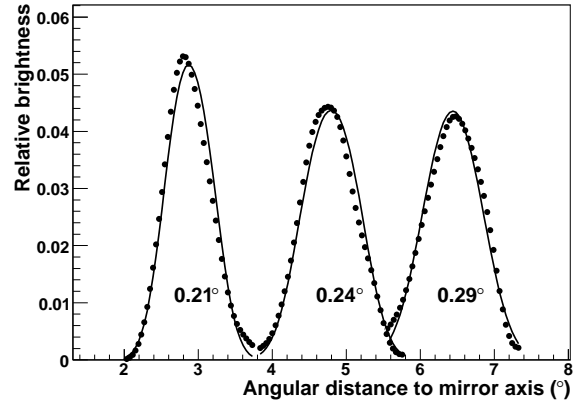


Figure 17: A star moves away from the center of the camera, and its light profile recorded by PMT is drawn in filled circles. The light profile described by a Gaussian function is drawn in a solid line. The sigma of Gaussian denotes that the spot size is also marked.

691 moves into the FOV of the tube, and steadily decreases
 692 when it moves away from the FOV, forming a light pro-
 693 file. The light profile can be fitted using a Gaussian
 694 function, whose sigma denotes the spot size. The spot
 695 size grows larger when the star moves away from the
 696 center of camera (Fig.17).

697 5. Summary

698 The telescopes were successfully run at YBJ from 711
 699 August 2008 up to July 2009. Millions of coincidence 712
 700 events with the ARGO-YBJ experiment have been col- 713
 701 lected. The performance of the telescopes was studied 714
 702 using these events. The trigger rate is about 0.5 Hz in 715
 703 stereo mode. Moreover, the mode energy of the tele- 716
 704 scope is 40 TeV when a pure proton composition is as- 717
 705 sumed.

706 The features of the two WFCTA prototype telescopes
 707 are summarized as follows:

- 708 • a 4.7 m^2 spherical mirror,
- 709 • a 16×16 PMT array covers an FOV of $14^\circ \times 16^\circ$
710 with 1° pixels,
- 711 • dual gain system for a dynamic range to 3.5 orders
712 of magnitude,
- 713 • DC coupling and modulized design for electronics,
- 714 • three-level online trigger logic: single channel trig-
715 ger based on S/N ratio, telescope trigger based on
716 pattern recognition, and event trigger for stereo-
717 scopic observation,

718 • maximized mobility and the telescope can be up-
719 lifted from 0° to 60° in elevation.

720 The absolute gains of the telescopes are calibrated us-
721 ing calibrated LEDs mounted at the centers of the mir-
722 rors. The systematic uncertainty of the calibration con-
723 stant is about 7%. The pixel gains are monitored on a
724 daily basis.

725 6. Acknowledgements

726 This work is supported by the Chinese Academy of
727 Sciences (0529110S13) and the Key Laboratory of Par-
728 ticle Astrophysics, Institute of High Energy Physics,
729 CAS. The Knowledge Innovation Fund (H85451D0U2)
730 of IHEP, China and the project Y0113G005C of NSFC
731 also provide support to this study.

732 We are very grateful to the ARGO-YBJ Collaboration
733 for authorizing us to use the data of the ARGO-YBJ
734 experiment.

735 We also acknowledge the essential support of H. M.
736 Zhang, W.Y. Chen, G. Yang, X.F. Yuan, C.Y. Zhao in
737 the installation, debugging, and maintenance of the de-
738 tector.

739 References

- 740 [1] V.I. Zatsepin et al., Nucl. Instr. and Meth. A 524 (2004) 196
741 195-207
- 742 [2] H.S. Ahn et al. Nucl., Instr. and Meth. A 579 (2007) 1034-1053
- 743 [3] Zhen Cao et al., A Future Project at Tibet: The Large High Al-
744 titude Air Shower Observatory (LHAASO), Chinese Physics C
745 2010, 34 (02): 249-252
- 746 [4] Huihai He et al., LHAASO Project: detector design and proto-
747 type, 31st ICRC, LODZ.(2009).
- 748 [5] Z. Cao et al., j. Phys. G: Nucl. Part. Phys. 31 (2005) 571
- 749 [6] He HuiHai et al., Proc. of 30th ICRC, Vol. 5 (2007) 949
- 750 [7] G. Aielli et al., Nuclear Physics B (Proc. Suppl.) 166 (2007)
751 96-102.
- 752 [8] J. Abraham et al., The Fluorescence Detector of the Pierre Auger
753 Observatory, Nucl. Instr. and Meth. A620 (2010) 227-251
- 754 [9] J. Abraham et al., Measurement of the energy spectrum of cos-
755 mic rays above 10^{18} eV using the Pierre Auger Observatory,
756 Phys. Letter B685 (2010) 239-246
- 757 [10] T.Nonaka et al., The present status of the Telescope Array ex-
758 periment, Nuclear Physics B (Proc. Suppl.) 190 (2009) 26-31
- 759 [11] J. Abraham et al., Nucl. Instr. and Meth. A 523 (2004) 50-95
- 760 [12] P. Bauleo et al., 29th International Cosmic Ray Conference Pune
761 (2005) 8, 5.8
- 762 [13] John H. Boyer et al., Nucl. Instr. and Meth. A 482 (2002) 457-
763 474
- 764 [14] D. Bird et al., Nucl. Instr. and Meth. A 349 (1994) 592-599
- 765 [15] T. Abu-Zayyad et al., 2001 ApJ 557 686
- 766 [16] S. P. Swordy, D. B. Kieda, arXiv:astro-ph/9909381v1
- 767 [17] G.Xiao et al., 29th International Cosmic Ray Conference Pune
768 (2005) 8, 21-24.
- 769 [18] L.P. Perera, Calibration of the Roving Xenon Flasher
770 with a Hybrid Photodetector internal HiRes report, 2003,
771 <http://www.cosmic-ray.org/papers/Lalith-Hpd.pdf>.

- 772 [19] GUO Yi-Qing et al, Chinese Physics C, 2010, 34 (5): 555-559
- 773 [20] Ma Ling-Ling et al, Geometry and optics calibration of WFCTA
774 prototype telescopes using star light, Chinese Physics C, pro-
775 ceeding.
- 776 [21] Hillas A. 1985, in Proc. 19nd I.C.R.C. (La Jolla), Vol. 3, p. 445.